Time- and Site- Resolved Dynamics in a Topological Circuit: Supplementary Material

Jia Ningyuan, Clai Owens, Ariel Sommer, David Schuster, and Jonathan Simon

Physics Department and James Franck Institute, University of Chicago

(Dated: April 5, 2015)

This supplement details the basic ideas behind creating an RF analog of a topological insulator. Because the RF lattice studied in this problem does not correspond to a tight-binding model, generating the band-structure and response functions is a bit more involved. What we have discovered in this work is that while our final circuit does not have a direct analog in other material systems, the essential feature, the local permutation of connections, results in a band-structure and dynamics that exhibit all of the signatures (both formally and experimentally) of a topological lattice model.

In section 1 we will describe, in a step by step manner, the transition from the theoretical, spinless, tight-binding Hofstadter model to the experimentally realized, spinful, network model. The changes that will have to be understood are: (1) Controlling the sign of the coupling by employing an un-grounded network topology, (2) Leaving the limit of weak inter-site coupling thereby coupling positive- and negative- energy excitations, (3)Employing strong inductive couplings vs. strong capacitive couplings. In section 2 we will introduce the computational tools that permit calculation of band-structures, edge modes, and Chern numbers. These tools employ network admittance tensors, and transcend the limit of a tight-binding Hamiltonian.

field, the system becomes periodic every Q unit cells [1]. This may be seen by writing out the tight-binding Hamiltonian, using the Peierl's substitution [1]:

$$
\begin{aligned}
H_{\text{Hofstadter}} = -t \sum_{m,n} a_{n,m} & \left(a_{n,m+1}^{\dagger} + a_{n,m-1}^{\dagger} \right. \\
& \left. + a_{n-1,m}^{\dagger} e^{im\phi} + a_{n+1,m}^{\dagger} e^{-im\phi} \right)
\end{aligned}
\tag{1}
$$

where t is the nearest neighbor tunneling rate, and $\phi = 2\pi P/Q$ is the magnetic flux per plaquette. It is clear that the new magnetic unit cell is Q lattice sites tall, as the exponential factor repeats ever Q lattice sites. The difficulty in implementing this Hamiltonian for uncharged particles, which thus do not respond directly to magnetic fields via a Lorentz force, is that $H_{\text{Hofstadter}}$ is not invariant under time reversal. This can be seen explicitly by verifying that the complex conjugate of $H_{\text{Hofstadter}}$ is not the same as $H_{\text{Hofstadter}}$ due to the complex exponential terms. Such a time-reversal asymmetric terms require something beyond inductors and capacitors (or equivalently, waveguides) to implement; possible approaches include periodic modulation [2–6] and coupling to materials with handed susceptibility induced by real magnetic fields [7].

FROM HARPER-HOFSTADTER TO LATTICE SPIN-HALL

The Harper-Hofstadter Model, and Breaking Time-Reversal Symmetry

When a massive particle is placed in a periodic 2D potential (lattice), its energy-momentum dispersion is modified by the lattice, forming bands of allowed and forbidden energies. Similarly, when a massive charged particle is placed in a uniform magnetic field, flat bands of allowed and disallowed energies, called Landau-levels, are formed. When both a lattice and a magnetic field are applied to a massive charged particle, the bands induced by the magnetic field and lattice compete- the resulting fractal band structure, as a function of magnetic field strength and energy, is known as the Hofstadter butterfly, and is shown in (SI Figure 1). The basic story is that if the magnetic field induces free-space cyclotron orbits whose area is a fully reduced rational P/Q lattice cells, then the band structure exhibits Q distinct bands (SI Figure 1). Equivalently, in the presence of a magnetic
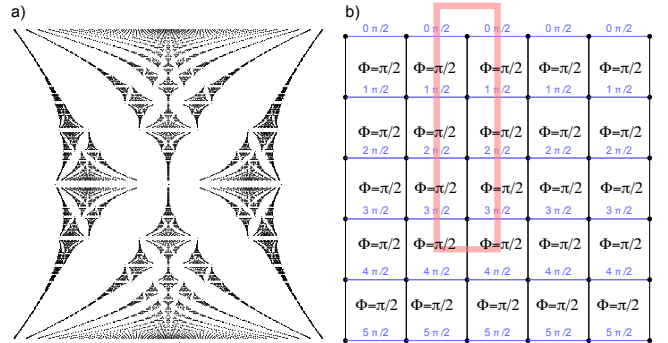

FIG. 1. (a) Hofstadter's butterfly: This figure shows the spectrum of allowed energies (vertical axis) versus magnetic flux per plaquette (horizontal axis), for a square lattice with uniform flux. (b) A particular gauge-choice for the Harper-Hofstadter model at a flux per plaquette of 1/4, corresponding to a geometric phase of $\pi/2$ acquired for tunneling counter-clockwise around a single plaquette. In the chosen gauge, all vertical tunneling has phase zero, and horizontal tunneling accrues of phase of $j\pi/2$, where j is the row. Because this phase is periodic every four sites, the new expanded unit cell, shown in red, is four sites tall.

Using Spin-Orbit coupling to recover Time-Reversal Symmetry

The simplest way to recover time-reversal symmetry is to add a second spin state that experiences the opposite magnetic field. Such physics typically arises due to Rashba or Dresselhaus spin-orbit coupling, after an appropriate gauge transformation and Peierls substitution [1]:

$$
\begin{aligned}
H_{\mathrm{SOC}} = -t \sum_{m,n} a_{n,m}(&a^{\dagger}_{n,m+1} + a^{\dagger}_{n,m-1} \\
&+ a^{\dagger}_{n-1,m} e^{im\phi S_z} + a^{\dagger}_{n+1,m} e^{-im\phi S_z})
\end{aligned}
\tag{2}
$$

The key point is that in the spinor model, the anti-unitary time-reversal operator not only takes a complex conjugate of the Hamiltonian, but also flips spins. Under such an operation it is clear that H_{SOC} is time-reversal invariant.

What this does not yet tell us is how to engineer a spin that flips under time-reversal. It turns out that for any system of two degenerate energy levels, there is a basis $(0,1)$ for which the basis-states are invariant under time-reversal, and a basis $(\uparrow,\downarrow)$ for which they swap.

The above can easily be seen using our experimentally realized system as an example: consider an excitation that may live in either of two resonant circuits A or B, as in the main text. In this case, reversing time certainly does not move the excitation from resonator A to resonator B. Thus the basis $(0,1)=(A,B)$. By contrast, if we choose an excitation that is in a rotating superposition of the two resonators, $(A \pm iB)/\sqrt{2}$, reversing time corresponds to taking a complex conjugate or equivalently reversing the rotation direction, and thus swaps the excitation. Thus $(\uparrow,\downarrow) = (A \pm iB)/\sqrt{2}$. This may also be seen by noting that the time-reversal operator is a unitary matrix times a complex conjugation operator [8] .

What we have shown is that a pseudo-spin degree of freedom may be engineered using simple, time-reversal-invariant linear components; the spin "flips" under time-reversal in an appropriately chosen basis. What remains, then, is to engineer an effective magnetic field that acts oppositely on the two spin states. All we have shown so far is that this should be possible without violating time-reversal symmetry, as the entire target system is time-reversal invariant.

Put another way- in the basis of the up- and down-pointing spins, the Hamiltonian will supply a time-reversal-symmetry breaking magnetic field to each spin state, corresponding to a Lorentz force. However, because the up- and down- pointing spin states themselves are time-reversal breaking quantities, the whole Hamiltonian does not violate time-reversal symmetry. This hints at the possibility perhaps such a Hamiltonian can be engineered from entirely linear, reciprocal components.

EXPERIMENTAL REALIZATION

To gain a quantitative understanding of the behaviors of a photon in a topologically non-trivial microwave circuit, it is instructive to return to the simple case of a lumped-element 1D transmission line and its generalizations.

Engineering Photon Dispersion in 1D Microwave/RF Lattices

1D Transmission Line: Light in a transmission line has a linear dispersion, reflecting the fact that information travels down the transmission line with a constant velocity $v = c/n$, where c is the speed of light in vacuum and n is the index of refraction of the transmission line. Such a system may be modeled by a capacitors which are coupled to one another by inductors, where the capacitor value is the given capacitance per unit length of the transmission line, and the inductor value is given by the inductance per unit length of the transmission line. We consider the more familiar case of sites that are grounded on one side (SI Figure 2). This lumped-element model has a linear dispersion at low momentum, reflecting the behavior of its continuum counterpart. As the momentum approaches the wave-vector of the lumped elements, the dispersion levels off: $\omega = 2\omega_0 \sin(q/2)$, with $\omega_0^2 = 1/LC$, with L and C the lumped inductance and capacitance respectively, and q the quasi-momentum in units of inverse lumped element sites.
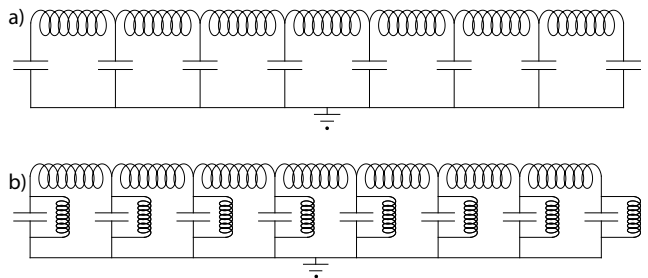

FIG. 2. (a) A grounded lumped-element model of a transmission line, with light-like dispersion at low-momenta, and a cutoff at a quasi-momentum given by the inverse of the inter-site spacing. (b) A grounded lumped-element model of a tight-binding lattice.

1D Tight-Binding Lattice for Photons: To make the photons appear "massive," an inductor $L_{\mathrm{site}} \ll L$ may be added in parallel with the on-site capacitors. In this case the system behaves not as a transmission line, but as a string of coupled resonators. These resonators have a "rest-mass" of $\omega_{\mathrm{res}}^2 = 1/(L_{\mathrm{site}}C)$ that rounds out the dispersion at low quasi-momenta, imbuing the photons with a mass:

$$\omega = 2\omega_0 \sqrt{\frac{L}{4L_{\text{site}}} + \sin^2(q/2)}$$

$$\approx 2\omega_0 \left(\frac{L}{4L_{\text{site}}}\right)^{1/2} (1 + \frac{L_{\text{site}}}{L}\sin^2(q/2)) \qquad (3)$$

in the limit $L_{\text{site}} \ll L$.

The width of the band is then $4\omega_0(L_{\text{site}}/4L)^{1/2}$. In a tight binding lattice the bandwidth is $4t$, where t is the nearest-neighbor tunneling rate. Thus we can now identify the tunneling rate as $t \approx \omega_0(L_{\text{site}}/4L)^{1/2}$.

Calculational Tools: The above expressions were computed from a more general frequency-domain approach, assuming a (frequency dependent) on-site impedance Z_{site} to ground, and a coupling impedance between sites Z_{couple}. From here the Kirchhoff's laws may be applied to the on-site voltages and inter-site currents to produce the following expression implicitly relating the frequency to the quasi-momentum: $4\sin^2(q/2) = -Z_{\text{couple}}(\omega)/Z_{\text{site}}(\omega)$.

Right- vs Left- Handed Circuits: With this more general frequency-dependent expression in hand, it is clear that swapping inductors and capacitors in these circuit networks is equivalent to sending $\omega \to \omega_0^2/\omega$ in the dispersion relation; such left handed transmission lines are well-studied [9], and their extension to two-dimension will be employed later in this work, in our discussion of the full topologically insulating circuit.

Grounded vs Symmetrical Networks: Zero Frequency Modes. It also bears mentioning that up to this point we have treated the on-site impedance network as grounded on one side; SI Figure 3 depicts the circuit symmetrically, without grounding, and indeed such a setup results in quantitatively identical behavior once Z_{site} is replaced by $Z_{\text{site}}/2$: The symmetrical case admits both even and odd solutions: the even solutions are all at zero frequency, corresponding to a DC shift at various quasi-momenta, and hence may be ignored, while the odd solutions are the same as those reached in the grounded circuit network. The symmetrical generalization will become important in the 2D system, where the sign of a site-to-site coupling may be reversed (made negative) by connecting the positive end of one site to the negative of the other, and vice-versa; in 1D such a choice can always be gauged away; not so in 2D: this is the origin of the spin-hall effect in our lattices.

Engineering Photon Dispersion in 2D Microwave/RF Lattices

In this section we will extend from 1D to 2D transmission lines, and add a spin degree of freedom, and finally a synthetic spin-orbit coupling. We will describe, along the way, the calculational tools necessary to compute 1)the modes of the infinite system, 2)the edge states in a strip with periodic boundary conditions at finite quasi-momentum and finally 3)the two-point couplings in a finite lattice.
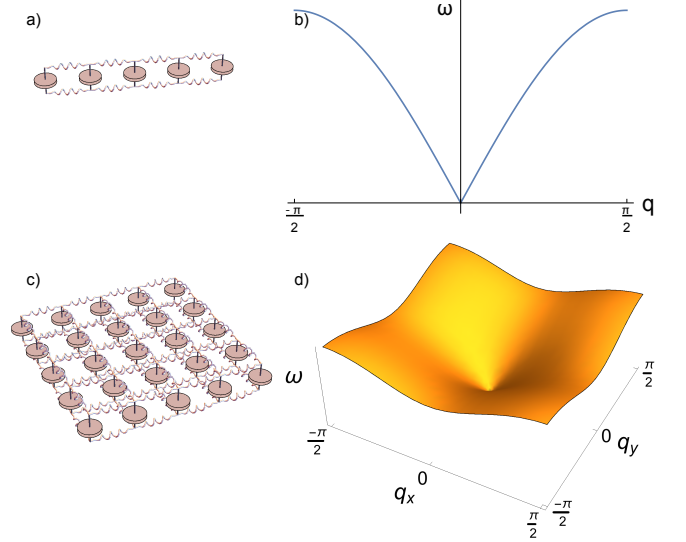

FIG. 3. (a) In the lumped-element model of a transmission line, the capacitance per unit length is modeled with an actual capacitor, and the inductance with an actual inductor. (b) This system has a linear (light-like) dispersion at low momenta, rolling off at a momentum given by the spacing of the lumped-elements. This roll-off reflects the fact that a the lumped-element system behaves differently the continuous transmission line once the dynamics probe the discreteness of the lumped-element system (absent in the continuous system). (c) The two-dimensional extension of this model exhibits (conical) light-like 2D dispersion (d). For symmetry with what follows, we draw double-ended connections between the capacitors; the calculations in this section assume that the lower-side of the capacitors are grounded.

A 2D microwave circuit: The direct extension of the transmission line to two dimensions is a square lattice of grounded capacitors connected to their nearest neighbors with inductors, as shown in the lower left panel of SI figure 3. The dispersion for such a system, shown in SI figure 3d, is given in general by: $4(\sin^2(q_x/2) + \sin^2(q_y/2)) = -Z_{\text{couple}}(\omega)/Z_{\text{site}}(\omega)$, or $\omega \cong \omega_0|q|$, for low momenta $q \ll \pi$ in the special case of on-site capacitors and coupling inductors. This dispersion corresponds to the dynamics of waves propagating in the plane transverse to the two plates of a parallel plate capacitor in short, the 2D analog of a waveguide or transmission line. Note that it is only isotropic at low momenta, where the sines can be expanded to linear order in their argument.

Again we can make the photons appear massive (both in the lowest allowed energy, and in their dispersion/dynamics) by adding an on-site inductor, and again we can compute the dispersion of the system with inductors and capacitors swapped by sending $\omega \to \omega_0^2/\omega$.

Adding a spin degree of freedom: To add a spin-degree

of freedom to the system, we simply make a second copy of the 2D lattice structure: now there are two capacitors on each site, which we will label A and B or red and blue, and initially A capacitors are coupled to A capacitors by inductors, and B capacitors to B capacitors by another set of inductors and no A-B couplings, as in SI figure 3. Because the A and B sublattices are uncoupled, the dispersion relation is the same as a single-spin-state 2D lattice, with a two-fold degeneracy.
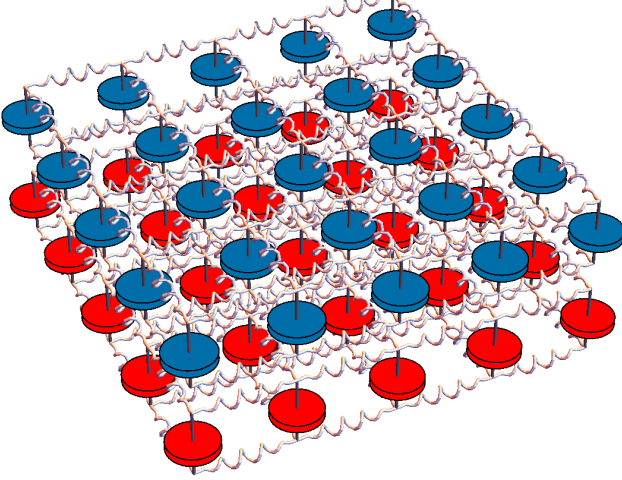

FIG. 4. Two-spin 2D photonic waveguide realized with discrete components. A photon in state A lives in the red lattice of capacitors, and a photon in state B lives in the blue lattice. The A- and B- lattices are uncoupled from one another.

Adding a synthetic spin-orbit coupling: To add the spin-orbit coupling, we must couple the A and B sublattices. As discussed in section 1 of this supplement, the states which map onto one-another under time reversal are $(\uparrow, \downarrow) = (A \pm iB)/\sqrt{2}$, and so it is these states which must experience synthetic gauge fields of opposite sign.

For simplicity, we will consider first the $\uparrow$ state, with a flux per unit cell of $\alpha = 1/4$: The Peierl's substitution dictates that we need to generate a tight-binding horizontal tunneling with a phase of $j\pi/2$, where j is the current row of the system. In the case of a "massless" photonic lattice, "tunneling" is not well-defined (the dispersion being linear at low momenta, rather than sinusoidal), so we will, for now, consider the massive case with the onsite inductor on each lattice site, and later send this onsite inductance to infinity.

A tunneling phase of $\pi/2$ sends the state $\uparrow = (A + iB)/\sqrt{2}$ on site 1 to the state: $e^{i\pi/2}(A+iB)/\sqrt{2} = (iA - B)/\sqrt{2}$ on site 2: in other words, the A resonator on site 1 needs to be inductively coupled to the B resonator on site 2 with a minus sign, while the B resonator on site 1 needs to be inductively coupled to the A resonator on site 2 without a minus sign. The beauty here is that

we never need to explicitly generate a complex tunneling matrix element (which we cannot do, as we cannot break time reversal with only lossless inductors and capacitors) as we are only transferring existing i's between A and B resonators on adjacent sites: this is the essence of time-reversal symmetric dynamics.

To realize the necessary negative tunneling matrix elements, it is be possible over a narrow bandwidth to couple with a capacitor instead of an inductor, thereby inverting the sign of the impedance. A more robust, broadband solution is to employ a double-ended, symmetric circuit topology, and inductively couple the top side of one resonator to the bottom side of the adjacent resonator. This approach is essential as we work in a maximally broadband configuration, by removing on-site inductors. As we will shortly show, this does not impact band topology. Finally we invert the circuit topology, swapping inductors and capacitors and sending $\omega \to \omega_0^2/\omega$. This is important, practically, to minimize the number of bulky inductors compared with the much smaller capacitors, and also does not impact the band topology. The circuit that was ultimately implemented is shown in SI figure 5.

Calculating Two-Point Transport Functions for a Finite System All of our numerics are based upon a frequency domain approach. We compute an admittance matrix $Y_{ij} = 1/Z_{ij}$, where Z_{ij} for $i \neq j$ is the direct impedance between nodes i and j. and Z_{ii} is the impedance between node i and gnd. It is very important to note that i and j are not spatial indices for an N by M lattice, i and j must each must take on $4NM$ unique values, corresponding to the NM lattice sites, with the two ends of each of two (A and B) inductors on each lattice site. The admittance matrix is thus $4NM$ by $4NM$.

Subject to a source current distribution $I_i^{\text{drive}}(\omega)$, Kirchhoff's laws for the voltage at node j, $V_j(\omega)$, provide $\sum_j Y_{ij}(\omega)V_j(\omega) = I_i^{\text{drive}}(\omega)$. We can thus solve for the voltage distribution according to: $V_i(\omega) = \sum_j (Y(\omega)^{-1})_{ij} I_j^{\text{drive}}(\omega)$.

In practice, we (inductively) inject a current at a single site μ, $I_j^{\text{drive}} = I_0 \delta_{j,\mu}$, and (inductively) measure the voltage at site ν, $V_\nu(\omega) = I_0 (Y(\omega)^{-1})_{\mu\nu}$. Thus the two-point transport information is entirely contained in the matrix elements of admittance tensor.

The ungrounded, symmetrical nature of the circuit results in infinite-frequency resonances of the admittance tensor preventing it from being inverted. While we could simply invert in the orthogonal subspace, in practice it is simple to include a vanishingly small capacitance from every node of the circuit to ground (which realistically arises from stray capacitances)- this moves the poles away from infinite-frequency, allowing inversion of the matrix; these high-frequency modes do not quantitatively impact the behavior of the circuit.
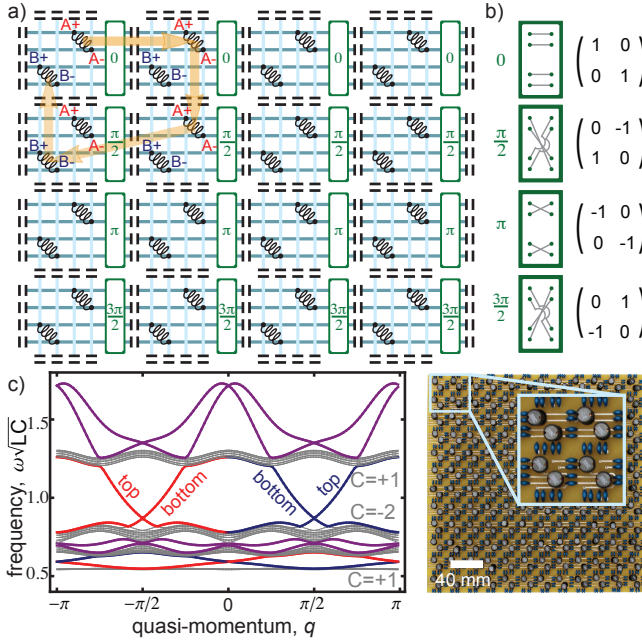
FIG. 5. (a) Circuit topological insulator schematic. The periodic structure is formed by onsite inductors and coupling capacitors, (black) that are connected via a latticework of wires (light and dark blue lines). At each lattice site, the two inductors "A" and "B" correspond to right and left circularly polarized spins. When a photon traverses a single plaquette (indicated in orange) it accumulates a Berry phase of $\pi/2$. The phase is induced by braiding (indicated by the green boxes and specified in b) of the capacitive couplings. (b) Structure of the coupling elements between lattice sites. Each row shows one of the four rotation angles implemented by the capacitive coupling in the circuit. The rotation angle (left column) is induced by connecting inductors as shown (middle column). The corresponding rotation matrices (right column) indicate the inductors being coupled, as well as the signs of the couplings. (c) Band Structure of a Circuit TI. A strip of circuit TI with fixed boundary conditions in the transverse direction is numerically diagonalized at finite longitudinal quasi-momentum q, yielding massive bulk bands (gray), and spin-orbit-locked edge states (red=↑, blue=↓) that reside in the bulk gap. Labels of "top" and "bottom" denote the boundary that each edge mode propagates along (with opposing group velocities $d\omega/dk$). The Chern numbers of the spin-up bands are indicated next to each band. The additional edge modes (indicated in purple) are not topologically protected. The highest energy edge-channel is localized to a single site along one direction, while the middle and lowest edge-channels are localized to two and three sites respectively. (d) Photograph of Circuit Topological Insulator. The inductors (black cylinders) are coupled via the capacitors (blue); circuit topology is determined by the trace layout on the PCB (yellow). Inset: Zoom-in on a single plaquette consisting of four adjacent lattice sites.
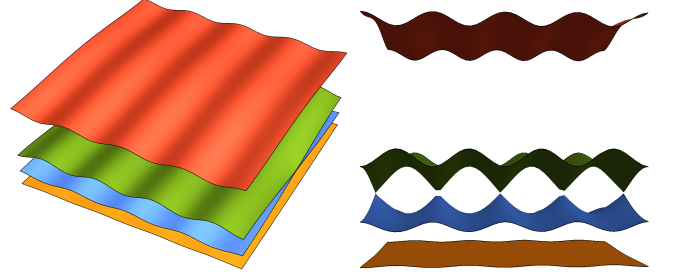

FIG. 6. Band structure for the topologically insulating circuits from two different perspectives (left/right), showing four distinct bands, with the middle two touching at four Dirac points. Note that each band is two-fold degenerate, for up- and down- spins.

Calculating Band-Structure in the Spin-Orbit Coupled Lattice

To compute the band-structure of the lattice, we consider a single "extended" (magnetic) unit cell containing a full flux quantum, which at a flux per plaquette of $1/4$, is a 1x4 strip of sites. We employ a circuit analog of Bloch's theorem, which amounts to a wave-function ansatz which is identical from one extended unit cell to the next up to a factor of $e^{\pm iq_x}$ in the $\pm x$ direction, and $e^{\pm iq_y}$ in the $\pm y$ direction. We can then apply Kirchhoff's laws to generate an admittance matrix $Y_{ij}(\omega, q_x, q_y)$ as a function of frequency and quasi-momentum. The mode frequencies are the roots of the determinant of Y, but computing these is computationally taxing, and will not provide the mode functions, which we will require for computation of the Chern numbers of the bands. A more general approach is to generate the equations of motion from Y. To this end we write $i\omega Y$ as a Laurent series in ω: $Y_{ij} = (1/i\omega L)_{ij} + i\omega C_{ij}$ It should be apparent (from the fact that Y gives the admittance between sites, which for a capacitor is $i\omega C$, and for an inductor is $1/i\omega L$) that C parameterizes the capacitive couplings, and L the inductive couplings. We can thus write the equations of motion in the time domain as: $\sum_{j,k} L_{ij} C_{jk} \ddot{V}_k + V_j = 0$

The mode frequencies are thus the square roots of the eigenvalues of the matrix $(LC)^{-1}$, and the bloch wave-functions are the corresponding eigenvectors. The numerically calculated band energies are plotted vs quasi-momenta q_x and q_y in SI figure 6.

Computing Band Chern Numbers: To numerically compute the Chern numbers of each of the up- and down-spin bands, we employ a gauge-independent definition of the Chern number:

$$C_b^{\uparrow,\downarrow} = \frac{1}{2\pi i} \int \int_{BZ} Tr\left(\rho^{\uparrow,\downarrow} \left[\frac{d\rho^{\uparrow,\downarrow}}{dq_x}, \frac{d\rho^{\uparrow,\downarrow}}{dq_y} \right] \right) d^2 q$$

with $\rho^{\uparrow,\downarrow}(q) \equiv \sum_b \left(\psi_b^{\uparrow,\downarrow}(q) \right)^\dagger \left(\psi_b^{\uparrow,\downarrow}(q) \right)$.

Here the sum over b runs through the bands under consideration: For the top and bottom bands, we compute their Chern numbers C_1 and C_4 independently. Because the middle two bands (2 and 3) touch (at Dirac points), their Chern numbers cannot be computed independently, so we must compute $C_{2,3}$ as a single entity. The above definition of the Chern number follows from the standard definition in [10] after a bit of algebra.

The $\psi_b^{\uparrow,\downarrow}(q)$ are the eigenvectors extracted from the band structure calculation in the previous section, with the added complication that we must project onto a single-spin subspace. To this end we compute eigenvectors and eigenvalues of $P^{\uparrow,\downarrow}(LC)^{-1}P^{\uparrow,\downarrow}$, with $P^{\uparrow,\downarrow} \equiv \frac{1}{2}\sum_l (A_l \pm iB_l)(A_l^\dagger \mp iB_l^\dagger)$, the projector onto the up- (down-) spin subspace. Here the A_l (B_l) are the state vectors corresponding to a voltage exclusively at the A (B) sub-lattice of site l.

It is worth noting that we have intentionally avoided bra-ket notation, typically employed in defining and computing Chern numbers; this was done to emphasize that all of the topological properties of the bands studied here are classical- the physics applies equally well to individual particle quantum wave-functions as to classical fields.

Calculating the Mode Structure of an Infinite Strip: The full 2D band-structure of a 2D system cannot exhibit edge-states, as the system has no edges! To study the properties of the edge states, we investigate the mode-structure of a strip of finite width, but infinite length; the top and bottom of the strip will now support edge modes, at the cost of projecting the resulting band-structure into one dimension.

To compute the spectrum of modes of our infinite strip, we employ the tools of the preceding section, but instead of diagonalizing a single magnetic unit cell with Bloch's theorem applied along both x and y, we only employ Bloch's theorem along x and consider a single strip of L unit cells along y with fixed boundary conditions at the top and bottom, defining the location of the edge. In practice this means that adjacent rows are assumed to be identical to the row under consideration, up to a factor of e^{iq_x}.

The result of such a diagonalization, versus quasi-momentum q_x, is shown in SI Figure 5c, with the bulk bands designated in gray and the edge states connecting them designated in red, blue, and purple. While edge states may exist in many systems, their existence is required if the sum of the Chern numbers of the bands below is non-zero (mod 2), and they are further guaranteed to be topologically protected, a hallmark of a topological insulator.

[1] Hofstadter, D. R. Energy levels and wave functions of Bloch electrons in rational and irrational magnetic fields. *Phys. Rev. B* **14**, 2239–2249 (1976). URL http://link.aps.org/doi/10.1103/PhysRevB.14.2239.

[2] Jotzu, G. *et al.* Experimental realisation of the topological Haldane model. *arXiv:1406.7874 [cond-mat, physics:quant-ph]* (2014). URL http://arxiv.org/abs/1406.7874.

[3] Lindner, N. H., Refael, G. & Galitski, V. Floquet topological insulator in semiconductor quantum wells. *Nat. Phys.* **7**, 490–495 (2011). URL http://www.nature.com/nphys/journal/v7/n6/abs/nphys1926.html.

[4] Wang, Y. H., Steinberg, H., Jarillo-Herrero, P. & Gedik, N. Observation of Floquet-Bloch States on the Surface of a Topological Insulator. *Science (80-.).* **342**, 453–457 (2013). URL http://www.sciencemag.org/content/342/6157/453http://www.ncbi.nlm.nih.gov/pubmed/24159040http://www.sciencemag.org/content/342/6157/453.abstracthttp://www.sciencemag.org/content/342/6157/453.full.pdf.

[5] Rechtsman, M. C. *et al.* Photonic Floquet topological insulators. *Nature* **496**, 196–200 (2013). URL http://www.nature.com/nature/journal/v496/n7444/fig_tab/nature12066_F1.html.

[6] Kitagawa, T., Berg, E., Rudner, M. & Demler, E. Topological characterization of periodically driven quantum systems. *Phys. Rev. B* **82** (2010). URL http://link.aps.org/doi/10.1103/PhysRevB.82.235114http://journals.aps.org/prb/abstract/10.1103/PhysRevB.82.235114.

[7] Wang, Z., Chong, Y. D., Joannopoulos, J. D. & Soljačić, M. Reflection-Free One-Way Edge Modes in a Gyromagnetic Photonic Crystal. *Phys. Rev. Lett.* **100** (2008). URL http://link.aps.org/doi/10.1103/PhysRevLett.100.013905.

[8] Shankar, R. *Principles of Quantum Mechanics* (Springer, New York, 2008), 1994. corr edn. URL http://www.amazon.co.uk/Principles-Quantum-Mechanics-R-Shankar/dp/0306447908.

[9] Caloz, C. & Itoh, T. Transmission line approach of left-handed (LH) materials and microstrip implementation of an artificial LH transmission line. *IEEE Trans. Antennas Propag.* **52**, 1159–1166 (2004). URL http://ieeexplore.ieee.org/xpl/login.jsp?tp=&arnumber=1296824&url=http://ieeexplore.ieee.org/xpls/abs_all.jsp?arnumber=1296824http://ieeexplore.ieee.org/xpl/articleDetails.jsp?arnumber=1296824.

[10] Hasan, M. & Kane, C. Topological insulators. *Rev. Mod. Phys.* **82**, 3045–3067 (2010). URL http://link.aps.org/doi/10.1103/RevModPhys.82.3045.